

● *Original Contribution*

A SINGLE-ENSEMBLE CLUTTER REJECTION METHOD BASED ON THE ANALYTIC GEOMETRY FOR ULTRASOUND COLOR FLOW IMAGING

WEI YOU and YUANYUAN WANG

Department of Electronic Engineering, Fudan University, Shanghai, China

(Received 7 January 2011; revised 3 May 2011; in final form 7 July 2011)

Abstract—In ultrasound color flow imaging (CFI), the single-ensemble eigen-based filters can reject clutter components using each slow-time ensemble individually. They have shown excellent spatial adaptability. This article proposes a novel clutter rejection method called the single-ensemble geometry filter (SGF), which is derived from an analytic geometry perspective. If the transmitted pulse number M equals two, the clutter component distribution on a two-dimensional (2-D) plane will be similar to a tilted ellipse. Therefore, the direction of the major axis of the ellipse can be used as the first principal component of the autocorrelation matrix estimated from multiple ensembles. Then the algorithm is generalized from 2-D to a higher dimensional space by using linear algebra representations of the ellipse. Comparisons have been made with the high-pass filter (HPF), the Hankel-singular value decomposition (SVD) filter and the recursive eigen-decomposition (RED) method using both simulated and human carotid data. Results show that compared with HPF and Hankel-SVD, the proposed filter causes less bias on the velocity estimation when the clutter velocity is close to that of the blood flow. On the other hand, the proposed filter does not need to update the autocorrelation matrix and can achieve better spatial adaptability than the RED. (E-mail: yywang@fudan.edu.cn) © 2011 World Federation for Ultrasound in Medicine & Biology.

Key Words: Ultrasound color flow imaging, Clutter rejection, Single-ensemble filter, Analytic geometry.

INTRODUCTION

To achieve accurate velocity estimates in ultrasound color flow imaging (CFI), it is essential to apply a high-performance filter to attenuate the clutter signals originated from surrounding tissues or vessel walls. Due to the high-energy of the clutter components and the limited number of transmitted pulses (Jensen 1996), the clutter rejection has been a challenging step in an ultrasound CFI system.

Conventionally, the digital high pass filter (HPF) is used as a common clutter rejection method. However, it is only applicable when the tissue is almost stationary since its frequency response is usually fixed (Bjærum et al. 2002b). To solve this problem, many adaptive clutter filters have been proposed in recent years. The down-mixing HPF (Thomas and Hall 1994; Brands et al. 1995) shifts the clutter spectrum to zero before applying a HPF. Then, Yoo et al (2003) and Yoo and Kim (2010) proposed a method that selects a HPF adaptively from a set of predefined filters. The eigen-based

filter is a group of clutter rejection methods, which involves the Karhunen-Loeve (K-L) expansion or other orthogonal decompositions techniques (Bjærum and Torp 1997; Ledoux et al. 1997; Kruse and Ferrara 2002; Bjærum et al. 2002a). These adaptive filters have shown great advantages over nonadaptive HPF because instead of a fixed response, their stopband are alterable according to the actual clutter Doppler frequency shift.

The eigen-based filters have been reviewed in detail recently (Yu and Løvstakken 2010) and it is pointed out that there are two basic types of eigen-based filters: the multi-ensemble approach such as the Eigenfilter (Bjærum and Torp 1997; Bjærum et al. 2002a) and the single-ensemble approach such as the Hankel-singular value decomposition (SVD) filter (Yu and Cobbold 2008). The review shows that the multi-ensemble approach is more suitable for scenarios where clutters are accelerated over the time or the tissue motion is uniform over the depth. On the other hand, the single-ensemble approach is more suitable for scenarios with highly spatially-varying tissue motions. In other words, the multi-ensemble filters have a good temporal adaptability and poor spatial adaptability while the single-ensemble filters have the exact opposite characteristics.

Address correspondence to: Prof. Yuanyuan Wang, Department of Electronic Engineering, Fudan University, Shanghai 200433, China. E-mail: yywang@fudan.edu.cn

Moreover, the recursive eigen-decomposition (RED) filter is developed as a compromise of the single and multi-ensemble approaches (You and Wang 2009, 2010). The RED could achieve a medium temporal and spatial adaptability at the same time.

Being the only implementation of the single-ensemble eigen-based clutter filter, the Hankel-SVD can achieve an outstanding spatial adaptability over the depth. However, it can provide at most half the number of eigen-components as can be obtained from the multi-ensemble approach. This limitation may make the Hankel-SVD less effective in representing clutters that span a wider spectrum (Yu 2007; Yu and Løvstakken 2010).

In this article we propose a single-ensemble eigen-based clutter rejection filter called the single-ensemble geometry filter (SGF). The SGF is derived from an analytic geometry point of view that gives a clearer physical interpretation of this algorithm. This proposed filter can achieve a spatial adaptability comparative to the Hankel-SVD. Meanwhile, it does not suffer from the number limitation of the eigen-components mentioned above and has a relatively good temporal resolution that is comparative to the Eigenfilter (Bjærum and Torp 1997; Bjærum et al. 2002a).

METHODS

Basic model

It is known that each slow-time ensemble demodulated from a sample volume is a complex vector \mathbf{x} containing M temporal samples. Variable M is the number of pulses transmitted at the same beam line that is also called the ensemble size. Usually, the vector \mathbf{x} can be synthesized by three components (Bjærum et al. 2002a):

$$\mathbf{x} = [x(0), x(1), \dots, x(M-1)]^T = \mathbf{c} + \mathbf{b} + \mathbf{w} \quad (1)$$

where \mathbf{c} , \mathbf{b} and \mathbf{w} are the clutter, blood flow and white noise component, respectively.

In this article, the clutter and blood flow components are modeled as simple complex exponential series with a designated basic frequency and a random phase shift. Then the m -th element of \mathbf{x} can be expressed by:

$$\begin{aligned} x(m) &= c(m) + b(m) + w(m) \\ &= k_c \exp(j(\omega_c m + \varphi_c)) + k_b \exp(j(\omega_b m + \varphi_b)) \\ &\quad + k_w w(m), \quad m = 0, \dots, M-1. \end{aligned} \quad (2)$$

where the subscript c , b and w denote the clutter, blood flow and noise, respectively; the variable k is the amplitude weight; the variable ω is the angular frequency shift determined by the velocity of object by using the Doppler equation; the variable φ is a random phase shift that subjects to a uniform distribution. It is important to point out that eqn (2) is the premise for our later analysis. All illustrations and derivations will be based on this model.

Interpretation from an analytic geometry perspective

Usually, the strength of the clutter component is much higher than the other two components (Torp 1997). Therefore, $x(m)$ can be approximated by:

$$x(m) \approx c(m) = k_c \exp(j(\omega_c m + \varphi_c)), \quad m = 0, \dots, M-1. \quad (3)$$

To visualize the processing procedure, we first start our discussion from the specific case with M equals 2. Let the horizontal and vertical axis refer to $x(0)$ and $x(1)$, respectively. One thousand points of $x(m)$ are simulated by (3) and plotted on a two-dimensional (2-D) plane. Note that for each simulated point, its $x(0)$ and $x(1)$ are dependent because the phase shift φ_c is deterministic. However, $x(0)$ or $x(1)$ for different two points are independent because their phase shifts φ_c are selected randomly. The data distribution is shown in Figure 1. Note that only the real part of $x(m)$ is used for visualization.

It can be observed from Figure 1 that the 2-D data distribution of $x(m)$ is a tilted ellipse that can also be regarded as a Lissajous figure under special cases. The first and second principal component directions are also plotted in Figure 1, which are almost the same as the directions of the major and minor axes of the ellipse. The ignorable difference is probably caused by the errors accumulated during numerical computations. Therefore, we consider using two deterministic directions of this ellipse instead of its principal components.

From the definition of the analytic Lissajous ellipse, it can be derived that the tilt angle of the ellipse will either be 45° (when $-\pi/2 < \omega_c < \pi/2$) or 135° (when $\pi/2 < \omega_c < 3\pi/2$). The detailed derivations can be found in

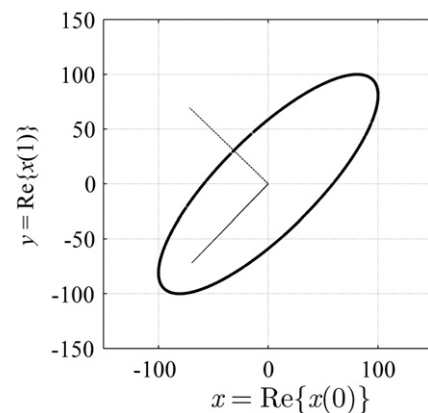


Fig. 1. Two-dimensional (2-D) data distribution of 1000 points of $x(m)$ with $m = 0$ and 1 (only the real parts are plotted, $k_c = 100$, $\omega_c = \pi/5$). The solid and dashed lines are the direction of the first and second principal component of these points, respectively, showing that for a 2-D situation, directions of the principal components are the same as directions of the ellipse's major and minor axes.

Appendix A. Therefore, the direction of the major axis of the ellipse is determined.

Generalization for multiple dimensions

When M equals 3, the ellipse becomes an ellipsoid in three-dimensional (3-D) space. The ellipse can no longer be visualized when $M > 3$, which unfortunately happens in most of the practical situations. Although 2-D geometry cannot work any more, linear algebra does not suffer from a dimension problem. In an M -dimensional space, a virtual “ellipse” is constructed by the means of linear algebra. According to Levy (1988), an M -dimensional “ellipse” can be represented in a quadratic form:

$$\sum_{p,q=0}^{M-1} a_{pq}x_px_q = C \quad (4)$$

where x_q is the dimension index, a_{pq} is the coefficients and C is a constant. The equation can also be put into a matrix form:

$$\mathbf{x}^T \mathbf{A} \mathbf{x} = C \quad (5)$$

$$\mathbf{A} = \begin{bmatrix} M-1 & -\exp(-j\omega_c) & -\exp(-j2\omega_c) & \cdots & -\exp(-j(M-1)\omega_c) \\ -\exp(j\omega_c) & M-1 & -\exp(-j\omega_c) & \cdots & -\exp(-j(M-2)\omega_c) \\ \vdots & \vdots & \ddots & \vdots & \vdots \\ -\exp(j(M-2)\omega_c) & \cdots & -\exp(j\omega_c) & M-1 & -\exp(-j\omega_c) \\ -\exp(j(M-1)\omega_c) & \cdots & -\exp(j2\omega_c) & -\exp(j\omega_c) & M-1 \end{bmatrix} \quad (8)$$

where the vector \mathbf{x} is $[x_0, x_1, \dots, x_{M-1}]^T$ and the matrix $\mathbf{A} = [a_{pq}]$. If \mathbf{A} is diagonal, (5) denotes the standard form. Otherwise, the standard form can be achieved by performing the singular value decomposition (SVD) on the matrix \mathbf{A} as long as it is symmetric positive definite.

$$\mathbf{x}^T (\mathbf{Q} \mathbf{\Lambda} \mathbf{Q}^T) \mathbf{x} = C \quad (6)$$

where \mathbf{Q} and $\mathbf{\Lambda}$ are the eigenvector and eigenvalue matrix of \mathbf{A} . In this case, the eigenvectors of \mathbf{A} define the principal directions of the ellipse and the inverse of the square root of the eigenvalues are the corresponding semi-axis lengths (Strang 1997).

Using Figure 1 as an example, we notice that $a_{00} = a_{11} = 1$ and $a_{01} = a_{10} = -\cos\omega_c$. Therefore,

$$\mathbf{A} = \begin{bmatrix} 1 & -\cos\omega_c \\ -\cos\omega_c & 1 \end{bmatrix} \quad (7)$$

Performing the SVD on the matrix \mathbf{A} with $\omega_c = \pi/5$ as an example, we get the second eigenvector of \mathbf{A} , $\mathbf{e}_2 = [0.707 \ 0.707]^T$, which shows a tilt angle of 45° . It is the same as what we pointed in the previous subsection. Note that the real matrix \mathbf{A} expressed by (7) is only for the theoretical derivation. For application, a complex version of matrix \mathbf{A} will be derived.

For an arbitrary M , the matrix $\mathbf{A} \in \mathbf{C}^{M \times M}$ (\mathbf{C} refers to the complex domain) can be expressed as follows (see Appendix B):

where ω_c is the Doppler frequency of the clutter component. For practice, an estimation of ω_c can be achieved using the auto-correlation algorithm (Kasai et al. 1985). The ω_c achieved here represents the mean clutter velocity during the time interval of M pulse echoes. An estimation

Table 1. Summary of steps of the SGF

Steps	Mathematic description
1. Input ensemble \mathbf{x}	
2. Estimate ω_c	$\omega_c \approx \angle \left(\frac{1}{M-1} \sum_{m=0}^{M-2} x^*(m)x(m+1) \right)$
3. Construct matrix \mathbf{A}	Refer to eqn (8)
4. Perform the SVD on \mathbf{A}	$\mathbf{A} = \mathbf{Q} \mathbf{\Lambda} \mathbf{Q}^H$
5. Rearrange columns of \mathbf{Q} (eigenvectors) according to the eigenvalues in ascendant order.	$\lambda_0 < \lambda_1 < \dots < \lambda_{M-1}$
6. Construct the filtering matrix (K_c is the filter order)	$\mathbf{F} = \mathbf{I} - \sum_{i=0}^{K_c-1} \mathbf{q}_i \mathbf{q}_i^H, \quad (\mathbf{q}_i \text{ is the } i\text{-th column of } \mathbf{Q})$
7. Output filtered ensemble	$\mathbf{y} = \mathbf{F} \mathbf{x}$

SGF = single-ensemble geometry filter; SVD = singular value decomposition.

Table 2. Summary of steps of the modified SGF

Steps	Mathematic description
1. Input ensemble \mathbf{x}	
2. Calculate the temporary variable a	$a = \sum_{m=0}^{M-2} x^*(m)x(m+1) / \sum_{m=0}^{M-2} x^*(m)x(m+1) $
3. Construct matrix $\mathbf{R}_{\text{ellipse}}$ using a	Refer to eqn (14)
4. Perform the SVD on $\mathbf{R}_{\text{ellipse}}$	$\mathbf{R}_{\text{ellipse}} = \mathbf{Q}\mathbf{\Lambda}\mathbf{Q}^H$
5. Rearrange the eigenvectors (columns of \mathbf{Q}) according to the eigenvalues in <i>descendant</i> order.	$\lambda_0 > \lambda_1 > \dots > \lambda_{M-1}$
6. Construct the filtering matrix (K_c is the filter order)	$\mathbf{F} = \mathbf{I} - \sum_{i=0}^{K_c-1} \mathbf{q}_i \mathbf{q}_i^H$, (\mathbf{q}_i is the i -th column of \mathbf{Q})
7. Output filtered ensemble	$\mathbf{y} = \mathbf{F}\mathbf{x}$

SGF = single-ensemble geometry filter; SVD = singular value decomposition.

bias of ω_c may lead to the bias of the blood velocity profile later. Up to now, we have constructed a harmonic matrix \mathbf{A} with the Toeplitz structure. The Toeplitz property implies the fact that only one dominant clutter frequency is modeled in our discussion, which has also been denoted by (2). The relationship between the eigenvectors of \mathbf{A} and the clutter frequency ω_c is shown intuitively in Figure 1. When ω_c is small, the eccentricity of the ellipse will be close to one. On the other hand, when ω_c is close to $\pm\pi/2$, the ellipse will degenerate into a circle in 2-D space with its eccentricity being zero. But for a greater M , the algorithm will always work because the principal components of a higher dimensional ellipse can always be determined even if ω_c equals $\pi/2$.

Once the matrix \mathbf{A} is obtained, the rest of the algorithm is almost the same as other eigen-based filters. The complete algorithm steps are summarized in Table 1. Note that the standard SVD is performed on the matrix \mathbf{A} without using any property of its Toeplitz structure.

Statistical perspective

For any eigen-based filter, it is inevitable to estimate the auto-correlation matrix \mathbf{R} first. By definition, \mathbf{R} is expressed by:

$$\mathbf{R} = E\{\mathbf{x}^H \mathbf{x}\} = \begin{bmatrix} r_0(0) & r_1^*(1) & \dots & r_{M-1}^*(M-1) \\ r_1(1) & r_1(0) & \dots & \dots \\ \vdots & \vdots & \ddots & r_{M-1}^*(1) \\ r_{M-1}(M-1) & \dots & r_{M-1}(1) & r_{M-1}(0) \end{bmatrix} \quad (9)$$

where

$$r_k(l) = E\{x(k)x^*(k-l)\}, \quad 0 \leq l \leq k \leq M-1 \quad (10)$$

with l being the lag number (Yu and Cobbold 2008). Substituting (3) into (10), we have:

$$r_k(l) = k_c^2 \cdot E\{\exp[j(\varphi_c + k\varphi_c)] \cdot \exp[-j(\varphi_c + (k-l)\omega_c)]\} = k_c^2 \exp(jl\omega_c) \quad (11)$$

The clutter frequency shift ω_c can be regarded as a mean value of the complex phase shifts between neighboring samples of the vector \mathbf{x} according to the classic auto-correlation estimation algorithm (Kasai et al. 1985):

$$\omega_c \approx \angle \left(\frac{1}{M-1} \sum_{m=0}^{M-2} x^*(m)x(m+1) \right) = \angle \left(\sum_{m=0}^{M-2} x^*(m)x(m+1) \right) \quad (12)$$

Substituting (12) into (11), we have $r_k(l) \approx k_c^2 \{\exp[j\angle(\sum_{m=0}^{M-2} x^*(m)x(m+1))]\}^l$. From this expression, we find that $r_k(l)$ is a complex number with an argument of $[\angle(\sum_{m=0}^{M-2} x^*(m)x(m+1))]^l$ and a modulus of k_c^2 , which gives:

$$r_k(l) \approx \begin{cases} k_c^2, & l=0 \\ k_c^2 \left(\frac{\sum_{m=0}^{M-2} x^*(m)x(m+1)}{\left| \sum_{m=0}^{M-2} x^*(m)x(m+1) \right|} \right)^l, & l \neq 0 \end{cases} \quad (13)$$

Let the temporary variable a equals $\sum_{m=0}^{M-2} x^*(m)x(m+1) / |\sum_{m=0}^{M-2} x^*(m)x(m+1)|$ and substitute (13) into (9), we get:

Table 3. Single-ensemble simulation parameters

Parameter	Value	
Ensemble size M	8	
Number of ensemble realizations N	100	
Scope of ω_c	0 to π	
Scope of ω_b	0 to π	
Increment step of ω_c , $\Delta\omega_c$	$\pi/12$	
Increment step of ω_b , $\Delta\omega_b$	$\pi/10$	
Amplitude of clutter k_c	100	40
Amplitude of blood k_b	10	10
Amplitude of noise k_w	1	5

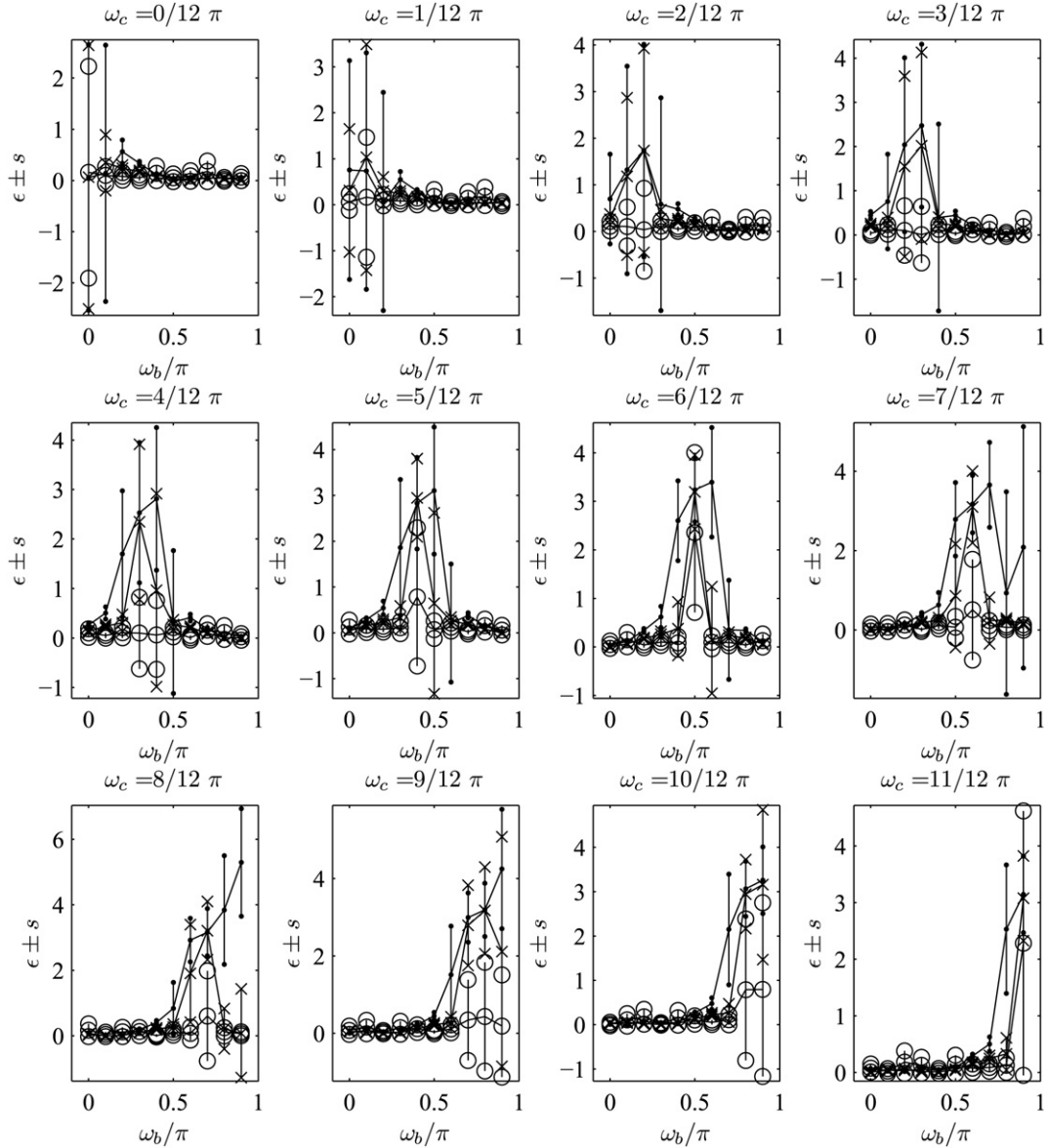


Fig. 2. Results of single-ensemble simulations after using the down-mixing high-pass filter (DM HPF), Hankel-singular value decomposition (SVD) and the single-ensemble geometry filter (SGF) (kc: kb: kw = 100:10:1).

$$\mathbf{R}_{\text{ellipse}} = \begin{bmatrix} 1 & a^{-1} & \dots & a^{-(M-1)} \\ a^1 & 1 & \dots & \vdots \\ \vdots & \vdots & \ddots & a^{-1} \\ a^{M-1} & \dots & a^1 & 1 \end{bmatrix} \quad (14)$$

Note that the scaling factor k_c^2 is ignored in (14) because it does not affect the eigenvectors of $\mathbf{R}_{\text{ellipse}}$.

Comparing (14) and (8), we notice that the matrix $\mathbf{R}_{\text{ellipse}}$ and \mathbf{A} are similar and the following relationship exists:

$$\mathbf{A} = M \cdot \mathbf{I}_{M \times M} - \mathbf{R}_{\text{ellipse}} \quad (15)$$

Equation (15) leads to a fact that eigenvectors of the matrix \mathbf{A} and $\mathbf{R}_{\text{ellipse}}$ are only different in the order (*i.e.*, if

their eigenvectors are organized according to correspondent eigenvalues in a descendant way, two sets of eigenvectors will be exactly reversed in the order). A modified SGF algorithm based on (14) has been derived from a statistical perspective and the steps are summarized in Table 2, which is slightly different from that described in Table 1. Note that these two approaches will achieve identical results but their physical interpretations are different.

SIMULATION RESULTS

Simulation studies are carried out to compare the performances of the proposed method to other popular clutter filters. All simulations are implemented in

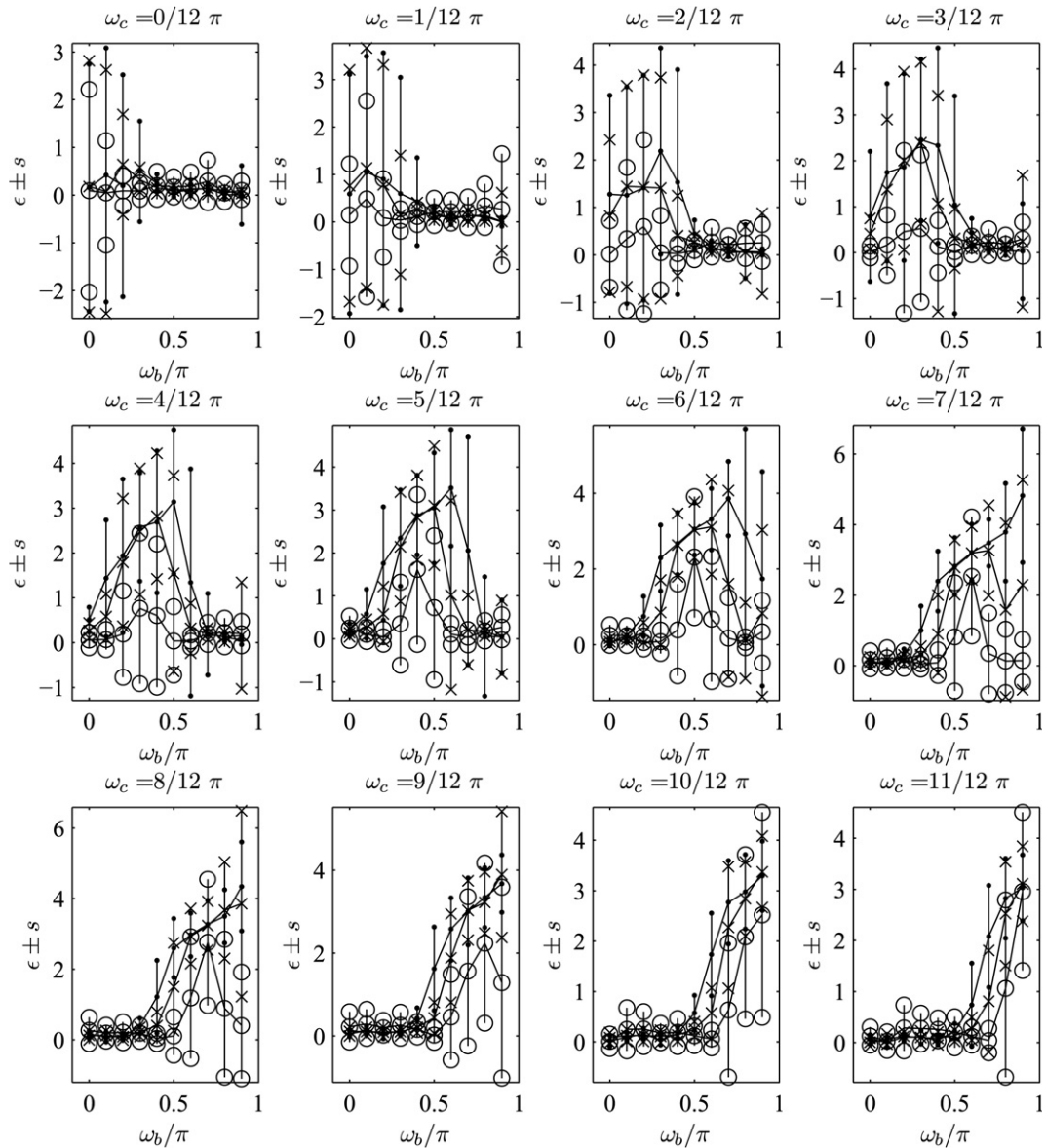


Fig. 3. Results of single-ensemble simulations after using the down-mixing high-pass filter (DM HPF), Hankel-singular value decomposition (SVD) and the single-ensemble geometry filter (SGF). (k_c : k_b : k_w = 40:10:5)

MATLAB R2010a (MathWorks, Natick, MA, USA) on a personal computer (AMD Athlon II 245-2.90 GHz, 2GB Memory).

Single-ensemble simulations

In this subsection, single-ensembles of \mathbf{x} are generated by (2) with different ω_c and ω_b . Three single ensemble clutter filters are applied to \mathbf{x} : the down-mixing (DM) HPF (a projection initialized, 3-order type-I Chebyshev IIR (Bjærum et al. 2002b), digital stop-band and passband frequencies are set to 0.02π and 0.2π , respectively), the Hankel-SVD (the frequency threshold f_{thr} set to 0.28, the clutter band Δf_{thr} set to 0.04) and the SGF filter (the clutter dimension K_c set to 1). All the filter

parameters used here are chosen by practical experience to ensure their best performances. Non-single ensemble clutter filters will be compared in the next subsection because only single ensemble data set can be synthesized by the simulation process proposed by Yu and Cobbold (2008). After the clutter rejection, the Doppler frequency shift of blood flow component $\hat{\omega}_b$ is estimated in each ensemble by the classic auto-correlation algorithm (Kasai et al. 1985). Suppose N realizations of \mathbf{x} are generated with random φ_c and φ_b , the mean value μ and standard deviation s of the estimated $\hat{\omega}_b$, are computed by:

$$\mu = \frac{1}{N} \sum_{i=1}^N \hat{\omega}_b(i) \quad (16)$$

Table 4. Multi-ensemble simulation parameters

Transducer center frequency f_0	5 MHz
Acoustic speed c	1540 m/s
F-number F_{num}	4
Repeated pulse number M	16
Beam-blow angle θ_b	45 degree
Beam-tissue angle θ_c	0
Tissue vibration frequency f_{vib}	5 Hz
Blood profile shape	parabolic
Vessel radius r_0	8 mm
Pulse repetition frequency f_{prf}	5 kHz
Transmitted cycle N_{cyc}	2.5
Maximum clutter-to-blood ratio CBR_{max}	42 dB
Minimum clutter-to-blood ratio CBR_{min}	40 dB
Maximum blood velocity v_{bmax}	0.35 m/s
Minimum clutter velocity v_{cmin}	0.2 m/s
Maximum clutter velocity v_{cmax}	0.3 m/s

$$s = \left(\frac{1}{N-1} \sum_{i=1}^N (\hat{\omega}_b(i) - \mu)^2 \right)^{\frac{1}{2}} \quad (17)$$

where $\hat{\omega}_b(i)$ is the estimated blood flow Doppler frequency shift of the i -th realization. The error between μ and theoretical ω_b can be obtained by $\varepsilon = \mu - \omega_b$. Table 3 lists all the simulation parameters.

Simulation results are plotted in Figures 2 and 3. The title for each subfigure is the value of ω_c in this ensemble, which has an increment step $\Delta\omega_c$ of $\pi/12$. The horizontal axis stands for ω_b and the vertical axis stands for $\varepsilon \pm s$.

In Figure 2, the amplitudes for the clutter, blood flow and noise components are 100, 10 and 1, respectively, to simulate the Doppler ensembles originated from an artery. Observing all subfigures, we can see that the smallest ε is achieved by the SGF (*i.e.*, closest to the horizontal axis), while the HPF has the largest ε . When ω_b is close to ω_c , the error and standard derivation will increase obviously. The worst estimate of $\hat{\omega}_b$ (*i.e.*, the largest μ) appears at the point when $\omega_b = \omega_c$. This phenomenon is easy to understand because when $\omega_b = \omega_c$, the clutter

and blood flow components have the same Doppler frequency shift and are mixed into one complex exponential series. The largest derivation of $\hat{\omega}_b$ also emerges at the point when $\omega_b = \omega_c$. In most cases, the derivations caused by then Hankel-SVD and the SGF are close, which are much better than that caused by the HPF.

Figure 3 plots the same results as Figure 2 only with different amplitude weights of the three components. The amplitudes of the clutter and blood flow get close and much stronger noises are included.

From Figure 3 we can see that the performances of the eigen-based filters deteriorate severely. Error arouses whenever ω_b is near ω_c and derivation of $\hat{\omega}_b$ is greater than that achieved in Figure 2. However, the error achieved by the proposed method is still lower than the other two filters obviously. From the above simulation results, we see that although the simulation model is simple, the major advantage of the proposed method has been shown effectively. A more complex simulation model considering the spectral broadening effect will be applied in the next subsection.

Multi-ensemble simulations

Comparisons of velocity profiles have been made in this subsection using simulated multiple ensembles along one beam line. The simulation procedure has been introduced in the recent paper (You and Wang 2009). The multi-ensemble simulation parameters are listed in Table 4.

Figure 4a depicts the theoretical profile and the estimated clutter velocity without any filtering. Figure 4b shows the clutter to blood ratio (CBR) variation along the depth.

Estimated profiles after applying the DM HPF, the Hankel-SVD, the RED method and the SGF are plotted in Figure 5. The filter type and order of the HPF are the same as those used in the subsection *single-ensemble simulations*. Its actual stopband and passband angular

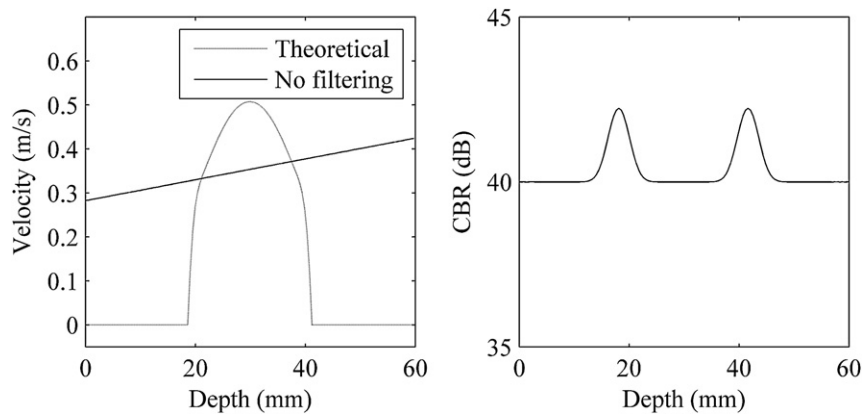


Fig. 4. (a) Clutter velocity before filtering and the theoretical blood profile. (b) The CBR variation along the depth.

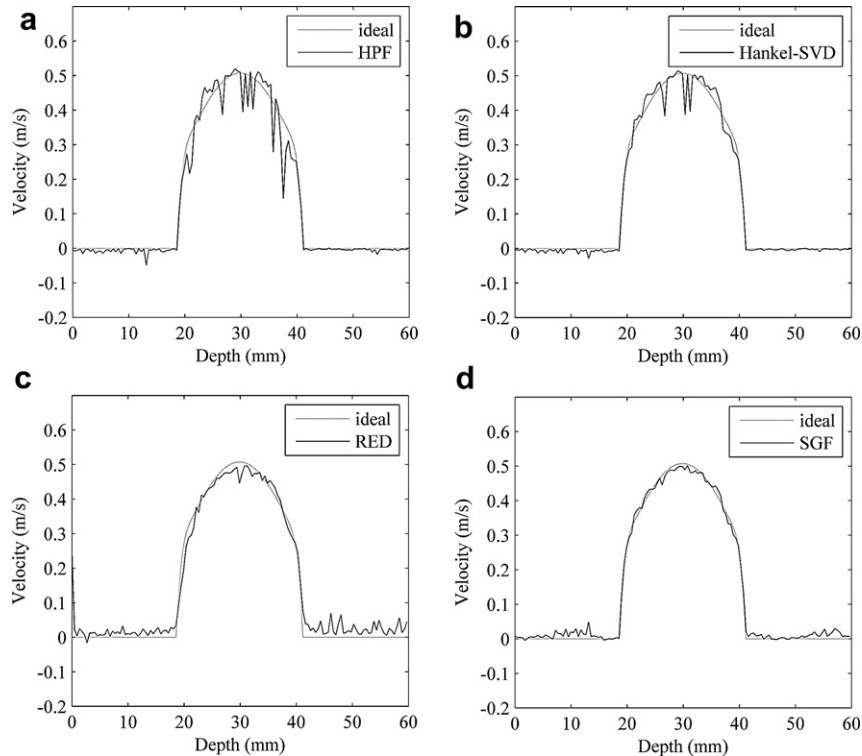


Fig. 5. Estimated profiles of multi-ensemble simulations after using the (a) down-mixing high-pass filter (DM HPF), (b) Hankel-singular value decomposition (SVD), (c) recursive eigen-decomposition (RED) and (d) single-ensemble geometry filter (SGF).

frequencies are set to 10 and 40 rad/s, respectively. For the Hankel-SVD, its f_{thr} and Δf_{thr} are set to 2000 and 100 Hz, respectively. For the RED, its filter order is one and the forgetting factor λ_{forget} is set to 0.9 and $\lambda_{\text{remember}}$ is set to 0.1. The filter order for the SGF is also set to one.

We can see from Figure 5 that the profiles achieved by the RED and the SGF are better than the other two methods. However, the first a few points obtained by the RED are severely biased because the multi-ensemble algorithm needs some time to converge after the initialization. Fortunately, the SGF does not suffer from the initialization problem and achieves the best blood profile.

IN VIVO RESULTS

Demodulated color flow imaging data were acquired from the carotid arteries of a healthy 25-year-old male volunteer using a commercial CFI system (ZONARE Medical Systems, Mountain View, CA, USA). The clutter rejection step in the CFI system was bypassed. Later different clutter filters were applied to evaluate their off-line performances. *In vivo* experimental settings are listed in Table 5. This study was approved by Fudan University's institutional review board.

The outcome CFI images after using five clutter filters are plotted in Figure 6 with all the color gains scaled to the same level. The HPF used is a projection initialized, 3-order Chebyshev type-I IIR with its pass-band and stopband cutoff frequency set to 10 Hz and 50 Hz, respectively. The frequency threshold f_{thr} and Δf_{thr} used for the Hankel-SVD are set to 500 and 100 Hz. The parameters used for the RED are the same as those used in the subsection *multi-ensemble simulations*. The clutter dimension K_c for the Eigenfilter and SGF is set to one manually. All the filter parameters are selected and adjusted by experimental experience to achieve their best performances.

Table 5. ZONARE CFI system parameters

Parameter	Value
Transducer center frequency	6 MHz
Pulse repetition frequency	1.428 kHz
Pulse number	14
Transmission pulse cycles	4 cycles
Lateral scan lines	257
Number of depth samples	142
Lateral field of view	-19.2~19.2mm
Axial field of view	1.8~20 mm

CFI = color flow imaging.

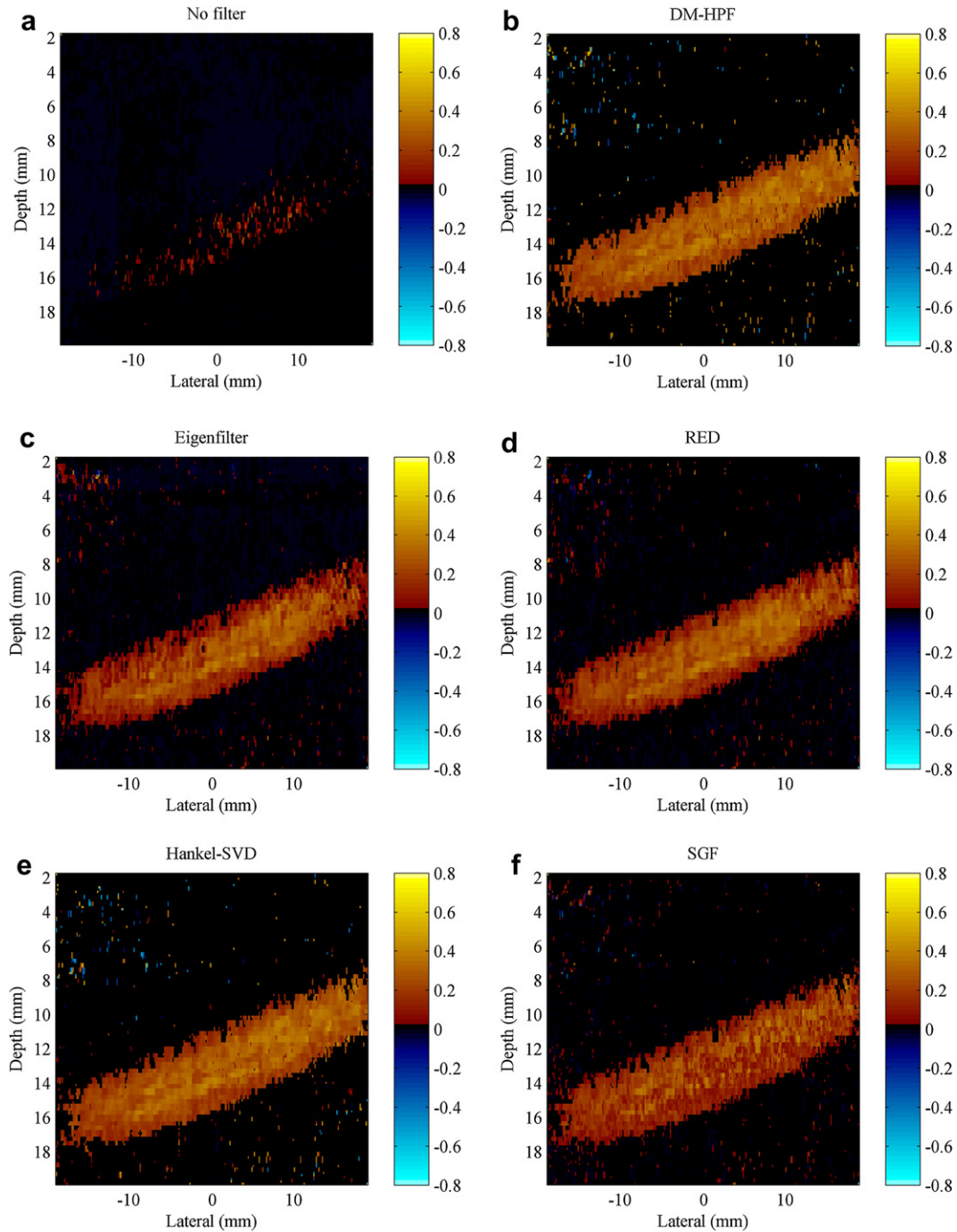


Fig. 6. *In vivo* color flow images after (a) no filtering, (b) down-mixing high-pass filter (DM HPF), (c) the Eigenfilter, (d) the recursive eigen-decomposition (RED), (e) the Hankel-singular value decomposition (SVD) and (f) the SGF. Unit for the color bar is m/s.

It can be seen from Figure 6a that the blood area is severely contaminated without any clutter filter applied. In Figure 6b–f, the vessel shape emerges but various degrees of velocity artifacts are brought in because of the side effect of clutter rejection. Relatively, the artifacts caused by the multi-ensemble methods are less than that caused by the single-ensemble ones. However, they must

rely on multiple ensembles near a certain depth where clutter motions are statistically stationary. On the other hand, the single-ensemble filters do not suffer from this limitation. In Figure 6f, it seems that the blood velocity around artery center is slower than those in the preceding four figures. Actually it is caused by the spatial adaptive capability of the SGF. In carotid artery scenario, the blood

Table 6. Summary of steps of the simplified SGF

Steps	Mathematic description
1. Input ensemble \mathbf{x}	
2. Calculate the temporary variable a	$a = \sum_{m=0}^{M-2} x^*(m)x(m+1) / \sum_{m=0}^{M-2} x^*(m)x(m+1) $
3. Construct vector \mathbf{q}_0 using a	$\mathbf{u}_1 = [1 \ a^1 \ a^2 \ \dots \ a^{M-1}]^T M^{-1/2}$
4. Perform the filtering	$\mathbf{y} = (\mathbf{I} - \mathbf{u}_1 \mathbf{u}_1^H) \mathbf{x}$

SGF = single-ensemble geometry filter.

power echoed from the artery center can be comparative to the clutter component. This will cause problem when applying the SGF filter because it uses the amplitude to differentiate between the blood and clutter components. If blood and clutter power are close, the SGF cannot work properly. Note that the Eigenfilter also uses amplitude to eliminate clutter. However, the Eigenfilter usually works in a batch mode and it has poor spatial resolution, which makes the signals from the artery center less influential to the whole data set.

DISCUSSION

Relationship with other eigen-based filters

All eigen-based filters require the estimation of the auto-correlation matrix, on which the orthogonal expansion is performed. The fundamental difference behind each eigen-based method is their various approaches to estimate this auto-correlation matrix.

For the multi-ensemble Eigenfilter, $r_k(l)$ is estimated by:

$$r_k(l) = \sum_{n=1}^N x_n(k)x_n^*(k-l) \quad (18)$$

where N is the number of ensembles used inside a certain depth window.

For the Hankel-SVD filter, $r_k(l)$ is estimated by each single ensemble (Yu and Cobbold 2008):

$$r_k(l) = \sum_{m=k+l}^{\frac{M}{2}+k+l} x(m)x^*(m-l) \quad (19)$$

Comparing (19) with (18), it is seen that the estimation is performed by the temporally stationary points within one ensemble instead of spatially stationary multiple ensembles along the depth.

For the SGF, $r_k(l)$ estimations are obtained by (13). It is different from the Hankel-SVD approach because an exponential clutter model is assumed as discussed in the subsection *basic model*. Using (13), an auto-correlation matrix with size M can be achieved. On the contrary, the size of the counterpart estimated by the Hankel-SVD is less than $M/2$. As more eigenvectors

can be extracted, each Doppler ensemble is decomposed into more orthogonal components and the proposed method can be more effective in representing clutters that span a wider spectrum. Notice that the SGF can only deal with sample volumes whose CBR is beyond zero. On the other hand, the Hankel-SVD filter can only deal with sample volumes where clutter velocity is below blood velocity when a frequency based dynamic order selection scheme is involved (Yu and Cobbold 2008).

Relationship with the down-mixing high-pass filter

The DM HPF proposed by Thomas and Hall is a “semi-adaptive” clutter filter. The input signal is first down-mixed using the estimated ω_c before applying a conventional HPF to remove clutter components. From Tables 1 and 2 we can see that ω_c is also estimated in the first step for the proposed SGF. Furthermore, in (8), a series of complex exponential values are utilized to construct the Toeplitz matrix \mathbf{A} . All these facts lead to an idea that the SGF may have links to the DM HPF.

Based on the derivations in Appendix C, we found that \mathbf{A} only has one nonzero eigenvalue λ_1 which equals M . The eigenvector corresponding to λ_1 is expressed by:

$$\mathbf{u}_1 = \frac{1}{\sqrt{M}} \begin{bmatrix} 1 \\ a^1 \\ \vdots \\ a^{M-1} \end{bmatrix} \quad (20)$$

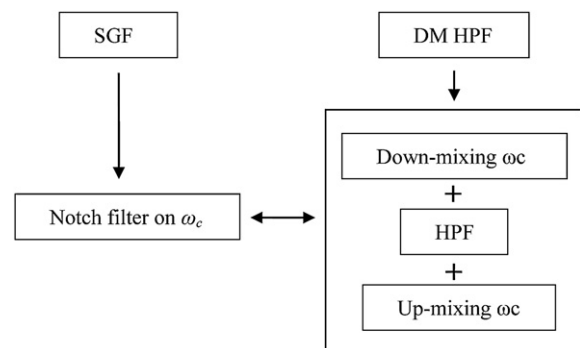


Fig. 7. Relationship between the single-ensemble geometry filter (SGF) and down-mixing high-pass filter (DM HPF).

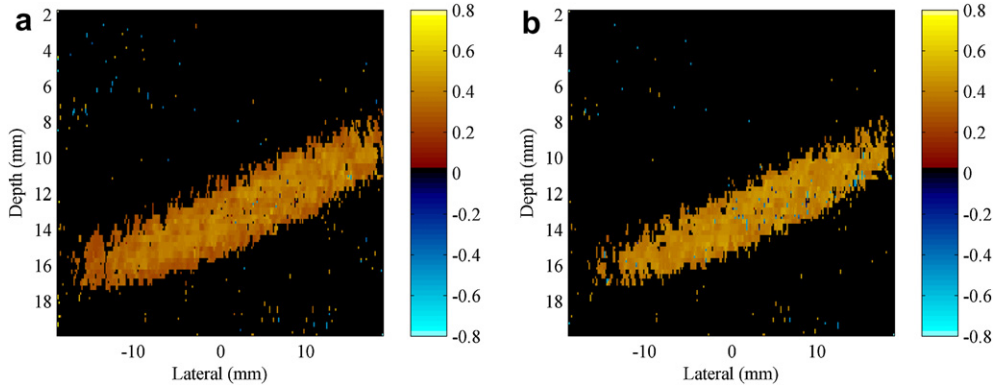


Fig. 8. *In vivo* color flow imaging (CFI) using down-mixing high-pass filter (DM HPF) with stopband and passband cutoff frequencies set to (a) 100 Hz and 200 Hz, order 5 (b) 200 Hz and 300 Hz, order 6. Unit for the color bar is m/s. Comparing to Figure 5, it can be seen that the down-mixing high-pass filter (DM HPF) is pretty sensitive to preset parameters such as stopband and passband cutoff frequencies, which shows another advantage of the single-ensemble geometry filter (SGF) filter.

Therefore, once we had the variable a defined in the subsection *statistical perspective*, the eigenvector \mathbf{u}_1 can be determined without involving any complicated matrix manipulation such as the SVD. Table 6 lists the steps for the final simplified version of SGF.

This simplified SGF is theoretically identical to the original and modified version of SGF described in Tables 1 and 2. However, the SVD is no longer needed, which will greatly release the time burden for the original SGF algorithm. In other words, the original SGF can be totally replaced by the simplified SGF without making any differences. Computational complexity comparison will be discussed in the next subsection.

The similarities between the SGF and DM HPF are: (1) they both require the estimation of clutter Doppler frequency shift ω_c beforehand; and (2) they both are single-ensemble filters.

The differences between the SGF and DM HPF are: (1) digital filter design specifications (*i.e.*, cutoff frequency, filter order *etc.*) are required for the DM HPF but not for the SGF; and (2) proper initialization techniques are required for the DM HPF but not for the SGF.

Eventually, the SGF can be regarded as an adaptive notch filter whose stopband is centered on the estimated

clutter Doppler shift ω_c . From this point of view, the SGF and DM HPF are working under a same framework. The links between the SGF and DM HPF can be depicted by Figure 7.

Comparing Figure 6a and f, it can be seen that when the stopband is narrow and around to zero, the effect of the DM HPF is close to that of the SGF as we expected. As the stopband cutoff frequency goes higher, more and more low velocity pixels are removed as shown in Figure 8a and b. Moreover, the DM HPF will cause an estimation bias toward higher velocities (CFI image becomes brighter) if a wide transition-band exists. On the other hand, the SGF does not suffer from these filter design uncertainties because it requires no input except for the Doppler ensemble.

Computational complexity

Generally, the computational complexity of the single-ensemble filter is higher than that of the multi-ensemble filter. It is because the single-ensemble filtering procedure has to be repeated for every sample volume along each beam line. On the other hand, the eigen-based methods are usually slower due to the SVD calculation.

Table 7. Computational complexity comparison

Clutter filter	Type	$O(M^x)$	$O(N^x)$	$O(M^x N^y)$	Time (s)
DM HPF	Single-ensemble	M^2	N^1	$M^2 N^1$	0.98
Eigenfilter	Multi-ensemble	M^3	N^1	$M^2 N^1$	0.12
Hankel-SVD	Single-ensemble	M^3	N^1	$M^3 N^1$	68.98
RED	Recursive	M^3	N^1	$M^3 N^1$	8.97
SGF (simplified)	Single-ensemble	M^2	N^1	$M^2 N^1$	1.55

DM = down-mixing; HPF = high-pass filter; SVD = singular value decomposition; RED = recursive eigen-decomposition; SGF = single-ensemble geometry filter.

Table 8. Requirements and properties of different clutter filters

Clutter filter	Type	Temporal stationary requirement	Spatial stationary requirement	CBR > 0 requirement	$\omega_b > \omega_c$ requirement	Auto-correlation matrix size
DM HPF	Single-ensemble	Low	Low	High	Low	N/A
Eigenfilter	Multi-ensemble	Low	High	Medium	Low	M
Hankel-SVD	Single-ensemble	High	Low	Low	High	No more than $M/2$
RED	Recursive	Low	Medium	Medium	Low	M
SGF	Single-ensemble	High	Low	High	Low	M

DM = down-mixing; HPF = high-pass filter; SVD = singular value decomposition; RED = recursive eigen-decomposition; SGF = single-ensemble geometry filter.

Suppose the ensemble size is M and the number of axial sample volume is N along each beam line, the complexity of the clutter filter is determined by not only M but also N (the number of CFI beam lines is not involved here because the applied clutter filters only use echo reflected from one direction). Table 7 lists the computational complexity of different clutter filters on the order of M , N and their cross term $M^x N^y$.

From Table 7 we can see that on the order of M , the complexities of the simplified SGF and DM HPF are lower than the others because it does not involve the SVD. On the order of cross term $M^x N^y$, the Eigenfilter is identical to the DM HPF because it does not need iteration for each beam line although it involves the SVD. For the rest two filters, their complexities are relatively high because they both require iterative calculations of the SVD. Using the same *in vivo* data, the actual time consumptions of different clutter filters for a complete CFI image are listed in the last column of Table 7. It can be seen that compared with the RED, time consumption of the SGF and Hankel-SVD is much lower. This is mainly because the Hankel-SVD is not implemented by the built-in SVD algorithm optimized by MATLAB. Compared with the Hankel-SVD and RED, the SGF is faster because it involves nothing but basic matrix operations. Interestingly, we notice that the eigen-based Eigenfilter is even faster than the DM HPF. This may be caused by two reasons: (1) with a small M applied in the CFI, the order of M does not affect the actual time consumption as much as the term N^x , or $M^x N^y$; and (2) the optimized SVD and matrix operations built in MATLAB greatly reduces the real-time consumption of the Eigenfilter. But for the single-ensemble filters, iterations are inevitable and may cause a lot of time consumption in MATLAB codes.

Based on all the discussions above, major requirements and properties of existing clutter filters are summarized in Table 8.

CONCLUSIONS

The eigen-based clutter filter consists of two general types: the multi-ensemble filter and the single-ensemble filter. The latter one can perform clutter rejection within

one sample volume and it is more suitable for CFI scenarios with highly spatial varying tissue motions (e.g., transthoracic coronary imaging) (Yu and Løvstakken 2010). However, as the only existing single-ensemble method, the Hankel-SVD decomposes each Doppler ensemble into less than $M/2$ components, which is not effective for sample volumes with complex clutter movements.

In this article, the single-ensemble geometry filter is proposed as a novel single-ensemble clutter rejection method. It is based on a simple exponential clutter model and it interprets the whole clutter suppression process from a geometry perspective, which gives us a more intuitive explanation of the proposed algorithm. The SGF has been validated by both simulations and *in vivo* experiments. Results show that the proposed method can achieve a great spatial adaptability and after proper simplification, its actual computational complexity is much lower than other eigen-based methods. More *in vivo* studies combined with turbulent flow and arterial stenosis will be carried in the future to further validate the effectiveness of the proposed method in clinical applications.

Acknowledgments—This work is supported by Natural Science Foundation of China (No.10974035) and the Program of Shanghai Subject Chief Scientist (No. 10XD1400600). The authors also wish to thank Dr. A. C. H. Yu (Department of Electrical and Electronic Engineering, University of Hong Kong) for providing clinical data of color flow images.

REFERENCES

- Bjærum S, Torp H. Optimal adaptive clutter filtering in color flow imaging. *IEEE Ultrason Symp Proc* 1997;2:1223–1226.
- Bjærum S, Torp H, Kristoffersen K. Clutter filters adapted to tissue motion in ultrasound color flow imaging. *IEEE Trans Ultrason Ferroelectr Freq Control* 2002a;49:693–704.
- Bjærum S, Torp H, Kristoffersen K. Clutter filter design for ultrasound color flow imaging. *IEEE Trans Ultrason Ferroelectr Freq Control* 2002b;49:204–216.
- Brands PJ, Hoeks APG, Reneman RS. The effect of echo suppression on the mean velocity estimation range of the RF cross-correlation model estimator. *Ultrasound Med Biol* 1995;21:945–959.
- Jensen JA. Estimation of blood velocity using ultrasound. A signal processing approach. New York: Cambridge University Press; 1996.

- Kasai C, Namekawa K, Koyano A, Omoto R. Real-time two-dimensional blood flow imaging using an autocorrelation technique. *IEEE Trans Sonics Ultrason* 1985;32:458–464.
- Kruse DE, Ferrara K. A new high resolution flow system using an eigendecomposition-based adaptive filter for clutter rejection. *IEEE Trans Ultrason Ferroelectr Freq Control* 2002;49:1384–1399.
- Ledoux LAF, Brands PJ, Hoeks APG. Reduction of the clutter component in Doppler ultrasound signals based on singular value decomposition: A simulation study. *Ultrason Imaging* 1997;19:1–18.
- Levy S. *Differential geometry: Manifolds, curves and surfaces*. New York: Springer Verlag; 1988.
- Strang G. *Introduction to linear algebra*. 2nd edition. Massachusetts: Wellesley-Cambridge Press; 1997.
- Thomas L, Hall A. An improved wall filter for flow imaging of low velocity flow. *IEEE Ultrason Symp Proc* 1994;3:1701–1704.
- Torp H. Clutter rejection filters in color flow imaging: A theoretical approach. *IEEE Trans Ultrason Ferroelectr Freq Control* 1997;44:417–424.
- Yoo YM, Kim Y. New adaptive clutter rejection for ultrasound color Doppler imaging: *In vivo study*. *Ultrason Med Biol* 2010;36:480–487.
- Yoo YM, Managuli R, Kim Y. Adaptive clutter filtering for ultrasound color flow imaging. *Ultrason Med Biol* 2003;29:1311–1320.
- You W, Wang YY. Adaptive clutter rejection for ultrasound color flow imaging based on recursive eigendecomposition. *IEEE Trans Ultrason Ferroelectr Freq Control* 2009;56:2217–2231.
- You W, Wang YY. A fast algorithm for adaptive clutter rejection in ultrasound color flow imaging based on the first-order perturbation: A simulation study. *IEEE Trans Ultrason Ferroelectr Freq Control* 2010;57:1884–1889.
- Yu ACH. Eigen-based signal processing methods for ultrasound color flow imaging. PhD dissertation, University of Toronto, 2007.
- Yu ACH, Cobbold RSC. Single-ensemble-based eigen-processing methods for color flow imaging-part I. the Hankel-SVD filter. *IEEE Trans Ultrason Ferroelectr Freq Control* 2008;55:559–572.
- Yu ACH, Løvstakken L. Eigen-based clutter filter design for ultrasound color flow imaging: A review. *IEEE Trans Ultrason Ferroelectr Freq Control* 2010;57:1096–1111.

APPENDIX A

The analytic Lissajous ellipse equation can be determined from the definition:

$$\begin{cases} x = \text{Re}\{x(0)\} = k_c \cos(\varphi_c) \\ y = \text{Re}\{x(1)\} = k_c \cos(\varphi_c + \omega_c) \end{cases} \quad (\text{A1})$$

Using the definition in (A1), we have the analytic ellipse equation in the plane x - y :

$$x^2 + y^2 - 2xy \cos \omega_c = k_c^2 \sin^2 \omega_c \quad (\text{A2})$$

To determine its tilt angle, we rotate the ellipse by θ degrees counter-clockwise. The relationship between the new x' - y' plane and the old x - y plane becomes:

$$\begin{cases} x = x' \cos \theta - y' \sin \theta \\ y = x' \sin \theta - y' \cos \theta \end{cases} \quad (\text{A3})$$

Substituting (A3) into (A2), we get:

$$(1 - 2\sin \theta \cos \theta \cos \omega_c)x^2 + (1 + 2\sin \theta \cos \theta \cos \omega_c)y^2 - 2(\cos^2 \theta - \sin^2 \theta) \cos \omega_c x' y' = k_c^2 \sin^2 \omega_c \quad (\text{A4})$$

To make (A4) standard, the coefficient before the term $x' y'$ has to be zero, which gives:

$$\theta = \frac{\pi}{4} + \frac{k\pi}{2}, \text{ or } \omega_c = \frac{\pi}{2} + k\pi, \quad (k = 0, 1, 2, \dots) \quad (\text{A5})$$

When ω_c is $\pi/2 + k\pi$, the ellipse becomes a circle. Otherwise, the tilt angle of the ellipse will be either 45° (when $-\pi/2 < \omega_c < \pi/2$) or

135° (when $\pi/2 < \omega_c < 3\pi/2$). Once the cross term $x' y'$ is removed, eqn (A4) becomes standard. Replacing $\sin \theta \cos \theta$ with $1/2$ (suppose $\theta = 45^\circ$) in (A4), we have:

$$\frac{x^2}{(k_c \sqrt{1 + \cos \omega_c})^2} + \frac{y^2}{(k_c \sqrt{1 - \cos \omega_c})^2} = 1 \quad (\text{A6})$$

Finally, we have a standard ellipse equation described by (A6) with its original tilt angle being 45° or 135° .

APPENDIX B

For an arbitrary M , we have the definition:

$$\begin{cases} x_0 = k_c \cos(\varphi_c) \\ x_1 = k_c \cos(\varphi_c + \omega_c) \\ x_2 = k_c \cos(\varphi_c + 2\omega_c) \\ \vdots \\ x_{M-1} = k_c \cos(\varphi_c + (M-1)\omega_c) \end{cases} \quad (\text{B1})$$

where x_0, \dots, x_{M-1} are the dimension indexes. Only real parts are included for simplification.

Select two equations arbitrarily from (B1):

$$\begin{cases} x_p = k_c \cos(\varphi_c + p\omega_c) \\ x_q = k_c \cos(\varphi_c + q\omega_c) \end{cases} \quad (\text{B2})$$

where $p, q = 0, 1, \dots, M-1$ and $p < q$. Using (A2), it can be derived from (B2) that

$$x_p^2 + x_q^2 - 2x_p x_q \cos(q-p)\omega_c = k_c^2 \sin^2(q-p)\omega_c \quad (\text{B3})$$

There will be $C_{M-1}^2 = M(M-1)/2$ equations defined by (B3) with different p and q in total. Summing up all these $M(M-1)/2$ equations, we get:

$$(M-1) \sum_{p=0}^{M-1} x_p^2 - 2 \sum_{\substack{p,q=0 \\ p < q}}^{M-1} x_p x_q \cos(q-p)\omega_c = k_c^2 \sum_{p=1}^{M-1} p \sin^2(M-p)\omega_c \quad (\text{B4})$$

Comparing (B4) and (4), we can determine the entries of the matrix \mathbf{A} . Let $a_{pq} = a_{qp}^*$, we get:

$$\mathbf{A} = \begin{bmatrix} M-1 & -\cos(\omega_c) & -\cos(2\omega_c) & \cdots & -\cos(M-1)\omega_c \\ -\cos(\omega_c) & M-1 & -\cos(\omega_c) & \cdots & -\cos(M-2)\omega_c \\ \vdots & \vdots & \ddots & \vdots & \vdots \\ -\cos(M-2)\omega_c & \cdots & -\cos(\omega_c) & M-1 & -\cos(\omega_c) \\ -\cos(M-1)\omega_c & \cdots & -\cos(2\omega_c) & -\cos(\omega_c) & M-1 \end{bmatrix} \quad (\text{B5})$$

It can be seen that (B5) is exactly the real part of (8). If we replace the cosine series in (B5) with complex exponential series, eqn (8) can be obtained finally.

APPENDIX C

According to the definition of variable a in subsection *statistical perspective*

$$a = \sum_{m=0}^{M-2} x^*(m)x(m+1) \left/ \sum_{m=0}^{M-2} x^*(m)x(m+1) \right| \quad (\text{C1})$$

where a is a complex number with unit modulus. Therefore, let

$$a = e^{j\theta} \quad (\text{C2})$$

where θ is an arbitrary augment. Substituting (C2) into (14),

Comparing (C4) to (C3), we get:

$$\begin{aligned}
 \mathbf{R}_{\text{ellipse}} &= \begin{bmatrix} e^{0j\theta} & e^{-j\theta} & \dots & e^{-(M-1)j\theta} \\ e^{j\theta} & e^{0j\theta} & \dots & \vdots \\ \vdots & \vdots & \ddots & e^{-j\theta} \\ e^{(M-1)j\theta} & \dots & e^{j\theta} & e^{0j\theta} \end{bmatrix} = \begin{bmatrix} e^{0j\theta} \\ e^{j\theta} \\ \vdots \\ e^{(M-1)j\theta} \end{bmatrix} \begin{bmatrix} e^{0j\theta} & e^{j\theta} & \dots & e^{(M-1)j\theta} \end{bmatrix}^* \\
 &= M \left(\begin{bmatrix} e^{0j\theta} \\ e^{j\theta} \\ \vdots \\ e^{(M-1)j\theta} \end{bmatrix} / \sqrt{M} \right) \left(\begin{bmatrix} e^{0j\theta} \\ e^{j\theta} \\ \vdots \\ e^{(M-1)j\theta} \end{bmatrix} / \sqrt{M} \right)^H
 \end{aligned} \tag{C3}$$

Due to the fact that $\mathbf{R}_{\text{ellipse}}$ is a Toeplitz matrix constructed by a series of complex exponential values, only the first eigenvalue will be nonzero (much larger than the other $M-1$ eigenvalues):

$$\begin{aligned}
 \mathbf{R}_{\text{ellipse}} &= \sum_{i=1}^M \lambda_i \mathbf{u}_i \mathbf{u}_i^H \\
 &= \lambda_1 \mathbf{u}_1 \mathbf{u}_1^H + \sum_{i=2}^M \lambda_i \mathbf{u}_i \mathbf{u}_i^H \\
 &\approx \lambda_1 \mathbf{u}_1 \mathbf{u}_1^H
 \end{aligned} \tag{C4}$$

$$\begin{cases} \mathbf{u}_1 = \frac{1}{\sqrt{M}} \begin{bmatrix} e^{0j\theta} \\ e^{j\theta} \\ \vdots \\ e^{(M-1)j\theta} \end{bmatrix} \\ \lambda_1 = M \end{cases} = \frac{1}{\sqrt{M}} \begin{bmatrix} 1 \\ a^1 \\ \vdots \\ a^{M-1} \end{bmatrix} \tag{C5}$$